Biosystems Engineering (2005) **90** (4), 369–379
doi:10.1016/j.biosystemseng.2004.12.011
PA—Precision Agriculture

Remote-sensing Technology for Vegetation Monitoring using an Unmanned Helicopter

Ryo Sugiura; Noboru Noguchi; Kazunobu Ishii

Graduate School of Agriculture, Hokkaido University, Kita-9, Nishi-9, Kita-ku, Sapporo, 060-8589, Japan; e-mail of corresponding author: ryosugi@bpe.agr.hokudai.ac.jp

(Received 10 February 2004; accepted in revised form 17 December 2004; published online 16 March 2005)

The objective of this study is to develop a system that can generate a map regarding crop status obtained by mounting an imaging sensor on an unmanned helicopter. The flight characteristic of an unmanned helicopter is effective for remote sensing. A real-time kinematic global positioning system (RTK-GPS) was adopted, and an inertial sensor (INS) that provides posture (roll and pitch angles) was installed in the helicopter. In addition, a geomagnetic direction sensor (GDS) that outputs an absolute direction was also attached to the helicopter. While obtaining pictures using the imaging sensor on the unmanned helicopter, image distortions arose due to changes in helicopter posture. Converting from image coordinates to global coordinates removes this distortion. However, a geomagnetic warp surrounding the helicopter created errors in the posture data, particularly a large GDS error. By correcting GDS errors, it was possible to generate a field map from helicopter-captured image data with a spatial error of 38 cm.

1. Introduction

Unmanned helicopters are smaller than full-scale manned helicopters and have been used primarily in agriculture, especially for chemical spraying (Wong, 2001; Agriculture, Forestry, Fishery and Aviation Association, 2002). The number of unmanned helicopters is increasing among large-scale farmers or contractors in Japan. However, an unmanned helicopter for agriculture is about one hundred thousand dollars, and almost same price as a 120 kW tractor. To justify the high cost of unmanned helicopters, helicopter manufacturers and farmers are seeking more ways to utilise them in agriculture. In this paper, unmanned helicopters are proposed as remote-sensing platforms for crop imaging. Precise crop sensing is one of the key issues in precision farming. Therefore, this technology would contribute to precision agriculture in Japan.

For sensing crop status in a field, satellite imaging (Inoue, 1997) and ground-based technology (Lee & Searcy, 1999) have both been studied. However, the spatial resolution of a satellite image is fairly low to acquire the leaf area index (LAI) which is very important value for crop growth estimation. It is also impossible to sense visible light during cloudy conditions. This is a significant problem, especially in Japan because June which is the growth period of some crops, such as rice and wheat, is the rainy season. Moreover, it usually takes 2 weeks or more for a satellite image to reach to customers.

On the other hand, ground-based sensing sometimes becomes unacceptable because the vehicle cannot get into a field of tall crops, such as maize. Also, the vehicle should not enter a field under muddy soil conditions due to soil compaction and vehicle immobility.

Remotely sensed images from aircraft (Senay *et al.*, 1998; Yang *et al.*, 2002) have been used in photogrammetry research. Aerial images typically have a spatial resolution of about 0·5 m and a spatial accuracy of about 1 m. The LAI of crops can be estimated from aerial images (Hu *et al.*, 2004). However, because such low resolution makes it difficult to segment crops and soil, the LAI cannot be acquired directly from aerial images.

Notation

a_k, b_k	Fourier coefficients
E_{FP}	final prediction error, deg^2
H_{True}	true value of the helicopter altitude, m
h	altitude of helicopter from the ground, m
N	number of direction data obtained by the geomagnetic direction sensor (GDS)
n	order of Fourier coefficients
$\boldsymbol{Q}_1$, $\boldsymbol{Q}_2$	rotation matrices for pan and tilt angles
$\boldsymbol{R}_1$, $\boldsymbol{R}_2$, $\boldsymbol{R}_3$	rotation matrices for roll, pitch and yaw angles
u, v	image coordinate system, pixel
x_c, y_c, z_c	position of the optical origin of the imaging sensor in the x_T, y_T, z_T system, m
x_G, y_G, z_G	image data position transformed to the global coordinate system, m
x_{gps}, y_{gps}, z_{gps}	GPS antenna position in the global coordinate, m
x_H, y_H, z_H	image data position in the helicopter coordinate system, m
x_{heli}, y_{heli}, z_{heli}	position of the optical origin of the imaging sensor in the global coordinate system, m
x_L, y_L, z_L	image data position in the local coordinate system, m
x'_L, y'_L, z'_L	projected point of image data to the ground plane in the local coordinate system, m
x_P, y_P, z_P	orthogonal coordinate system containing the pan rotation axis, m
x_T, y_T, z_T	orthogonal coordinate system containing the tilt rotation axis, m
Δx, Δy, Δz	GPS offset from the GPS antenna to the optical origin of the imaging sensor, m
α, γ, δ	bias to correct heading, pitch and roll angles, deg
β	bias to correct altitude data, m
ε	direction error of the geomagnetic direction sensor (GDS), deg
ϕ, θ, ψ	roll, pitch and yaw angles of the helicopter, deg
ϕ_{True}, θ_{True}, ψ_{True}	true value of roll, pitch and yaw angles, deg
μ	angle of view of the imaging sensor, deg
ρ_1, ρ_2	pan-head rotation angles about pan and tilt directions, deg
σ^2	variance of the prediction error of the yaw angle, deg^2
ω_{IMU}	relative yaw angle of the inertial measurement unit (IMU), deg
$\boldsymbol{\xi}_1$	vector from the x_P, y_P, z_P system to the x_T, y_T, z_T system of the pan-head, m
$\boldsymbol{\xi}_2$	vector from the GPS antenna to the x_P, y_P, z_P system, m
ψ_{GDS}	absolute yaw angle of the geomagnetic direction sensor (GDS), deg

If a small, readily manoeuvrable, low-altitude aerial platform (*e.g.* unmanned helicopter) could be introduced as a tool for crop status sensing, it would offer significant advantages over remote-sensing methods. As is generally known, the aerial manoeuvrability of a helicopter exceeds that of an aircraft. A helicopter can cruise in any direction and vertical take-off and hover flight are also possible (Kato *et al.*, 1982; Hongoh *et al.*, 2001). These abilities provide more flexibility as well as more efficiency for remote sensing. Unmanned helicopters can improve the resolution of manned airborne-based sensing due to their low flight altitude. Another benefit in using unmanned helicopters is that they can be operated by farmers themselves. It allows them to obtain imagery almost immediately. Thereby, the obtained data can be instantly used for crop production management and precision farming, such as variable rate technology.

The objective of this study is to develop a system that can generate a precise field map of crop information using images taken from an unmanned helicopter. This study employed helicopter position and posture data as external sources to transform image coordinates to global coordinates. In this study, the universal transverse Mercator (UTM) coordinate system was adopted as the global coordinate system. The UTM coordinates can be obtained from the world geodetic system (WGS84). Generating the precise field map without setting ground-control points requires accurate measurements of position and posture of a helicopter. Geometric distortions that occur in images taken from a helicopter are due to variations in position and posture (Gonzalez & Woods, 1993; Poli, 2001; Xu & Li, 2000). Therefore, a real-time kinematic global positioning system (RTK-GPS) was adopted as a positioning sensor, in addition to an inertial sensor (INS) and a geomagnetic direction sensor (GDS). Although a GDS provides absolute direction from north, large errors arise from magnetic influences of mechanical and electrical systems (Yukumoto & Matsuo, 1996). It is

necessary, therefore, to correct GDS data to generate a map based on the global coordinate system. A method to correct geometric image distortions and GDS output was developed. The spatial accuracy of the transformed and undistorted imagery was evaluated.

2. System components

Figure 1 shows the configuration of the helicopter system used in this study. The test helicopter has an engine displacement of 248 m*l*. The weight is 61·5 kg with an installed capacity of 15·8 kW and a payload of 300 N. This unmanned helicopter is an industrial product for agricultural spraying. In this research, all equipment used for spraying, such as its chemical tank and spray nozzles, were removed. An adjustable pan-head to mount an imaging sensor was installed under the fuselage. The pan-head can be controlled for both pan and tilt directions. Each rotation angle of the pan-head was measured by encoders.

The test imaging sensor was attached to the pan-head. An imaging sensor was a camera which contains three separate optical paths and charge-coupled devices (CCD). Images were captured by the sensor with a resolution of 640 by 480 at 8 bit/pixel. Special optical filters were installed over the sensors providing three video channels of green (G), red (R) and near infrared (NIR). The sensors can acquire each image with 15 frames/s. These three channels have centre wavelengths of 550, 650 and 800 nm and bandwidth of approximately 40 nm for each channel. These images have been used for detection of nitrogen contents and chlorophyll contents. Moreover, they can be the parameters of normalised vegetation index (NDVI) or green NDVI (Noh *et al.*, 2004; Chen *et al.*, 2003). The exposure time in each channel can be controlled through a serial interface of the recommended standard 232 C (RS-232C) to obtain a high-quality image for processing. The exposure time controller tries to keep average grey level in each channel of an image around 128 that is median

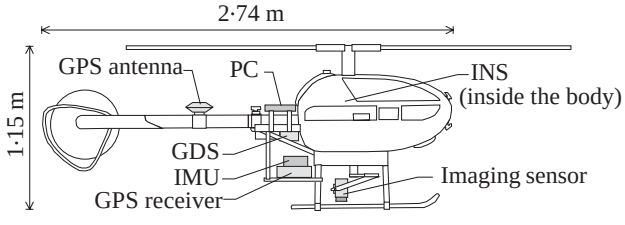

Fig. 1. Dimension of the test helicopter and the placement of instruments: GDS, geomagnetic direction sensor; GPS, global positioning sensor; IMU, inertial measurement unit; INS, inertial sensor; PC, personal computer

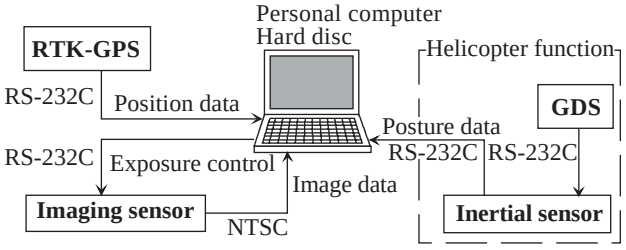

Fig. 2. Schematic diagram of the sensing system: GDS, geomagnetic direction sensor; RTK-GPS, real-time kinematic global positioning system; NTSC, video signal defined by the national television system committee; RS-232C, serial interface of the recommended standard 232 C

value of 8-bit image. As this imaging sensor was equipped with an optical lens with a small view angle, the internal distortion caused by the optical system was ignored.

The INS and the GDS were installed on the helicopter, with the INS providing roll and pitch angles of the platform, and the GDS providing absolute orientation. All of this posture data could be obtained at a rate of 10 Hz. A GPS antenna was mounted on the tail boom and a receiver was mounted on the rear fuselage. Position, posture, and pan-head data could be simultaneously acquired with the image data. Once received, all of the data was backed up on a personal computer (PC) located in the tail boom using an RS-232C connection. *Figure 2* shows the layout of these components.

An inertial measurement unit (IMU) that can measure roll, pitch, and yaw was also mounted with the GPS receiver. The IMU data was used as a reference for GDS calibration. Since an IMU is a precise posture sensor composed of three-axis optical fiber gyroscopes, it helps verify inertial measurement accuracy.

3. Methods

3.1. *Offset correction for the global positioning system*

To consider changes in the helicopter posture, it was necessary to correct GPS data from the position of the GPS antenna with respect to the optical origin of the imaging sensor. As seen in *Fig. 3*, the helicopter coordinate system (x_H, y_H, z_H) was defined as right-handed with the Y_h axis in the helicopter forward direction, and the Z_h axis pointing in the zenith direction. The rotation angles are pitch angle θ, roll angle ϕ and yaw angle ψ. Eulerian angles were adopted for describing the posture of helicopter. Therefore, the transformation matrices $\boldsymbol{R}_1$, $\boldsymbol{R}_2$, and $\boldsymbol{R}_3$ of each rotation

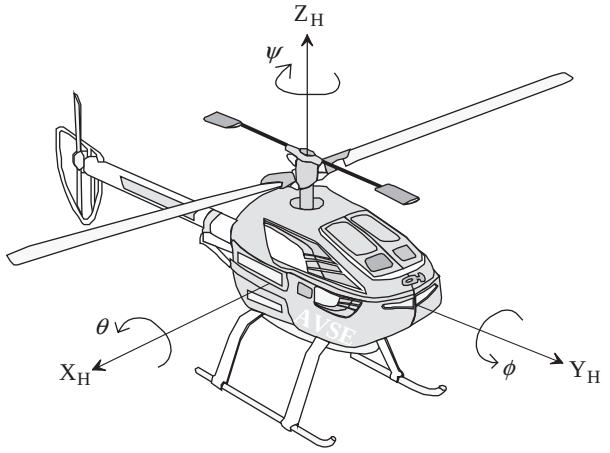

Fig. 3. Axes for a helicopter coordinate system: ϕ, θ, ψ, roll, pitch and yaw angles

angle can be expressed as follows:

$$\boldsymbol{R}_1(\phi) = \begin{pmatrix} \cos\phi & 0 & \sin\phi \\ 0 & 1 & 0 \\ -\sin\phi & 0 & \cos\phi \end{pmatrix}$$

$$\boldsymbol{R}_2(\theta) = \begin{pmatrix} 1 & 0 & 0 \\ 0 & \cos\theta & -\sin\theta \\ 0 & \sin\theta & \cos\theta \end{pmatrix}$$

$$\boldsymbol{R}_3(\psi) = \begin{pmatrix} \cos\psi & \sin\psi & 0 \\ -\sin\psi & \cos\psi & 0 \\ 0 & 0 & 1 \end{pmatrix} \quad (1)$$

The pan-head can rotate for pan and tilt directions and encoders can measure rotation angles around each direction. The test pan-head has two coordinate systems (*Fig. 4*). One is a x_P, y_P, z_P system whose Z_P axis corresponds with a pan rotation axis; another is a x_T, y_T, z_T system whose X_T axis corresponds with a tilt rotation axis. When ρ_1 is the pan angle rotation and ρ_2 is the tilt angle of the pan-head, the rotation matrices denoted by $\boldsymbol{Q}_1$ and $\boldsymbol{Q}_2$ are expressed by

$$\boldsymbol{Q}_1(\rho_1) = \begin{pmatrix} \cos\rho_1 & \sin\rho_1 & 0 \\ -\sin\rho_1 & \cos\rho_1 & 0 \\ 0 & 0 & 1 \end{pmatrix}$$

$$\boldsymbol{Q}_2(\rho_2) = \begin{pmatrix} 1 & 0 & 0 \\ 0 & \cos\rho_2 & -\sin\rho_2 \\ 0 & \sin\rho_2 & \cos\rho_2 \end{pmatrix} \quad (2)$$

A vector from the x_P, y_P, z_P system to the x_T, y_T, z_T system is $\boldsymbol{\xi}_1$; a vector from the GPS antenna to x_P, y_P, z_P system is $\boldsymbol{\xi}_2$; and a position of the optical origin of the imaging sensor is (x_c, y_c, z_c) in the x_T, y_T, z_T system. The corrected values of the GPS offset $(\Delta x, \Delta y, \Delta z)$ can be calculated by the following method:

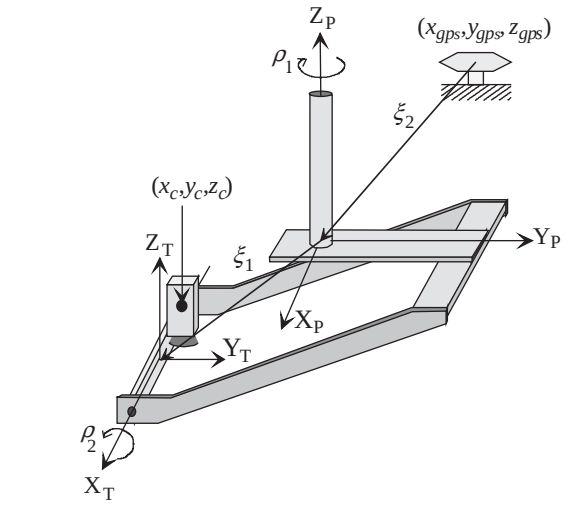

Fig. 4. Pan-head coordinate systems and rotation axes: (x_c, y_c, z_c), position of the optical origin of the imaging sensor; $(x_{gps}, y_{gps}, z_{gps})$, GPS antenna position; $\boldsymbol{\xi}_1$, vector from x_P, y_P, z_P system to the x_T, y_T, z_T system; $\boldsymbol{\xi}_2$, vector from the GPS antenna to the x_P, y_P, z_P system

$$\begin{pmatrix} \Delta x \\ \Delta y \\ \Delta z \end{pmatrix} = \boldsymbol{R}_3(\psi)\boldsymbol{R}_2(\theta)\boldsymbol{R}_1(\phi) \left(\boldsymbol{Q}_1(\rho_1) \;\middle|\; \boldsymbol{\xi}_2 \right) \left(\begin{array}{ccc|c} & \boldsymbol{Q}_2(\rho_2) & & \boldsymbol{\xi}_1 \\ \hline 0 & 0 & 0 & 1 \end{array} \right) \begin{pmatrix} x_c \\ y_c \\ z_c \\ 1 \end{pmatrix} \quad (3)$$

Therefore, using the position of the GPS antenna $(x_{gps}, y_{gps}, z_{gps})$, the optical origin of the imaging sensor $(x_{heli}, y_{heli}, z_{heli})$, in the global coordinate system can be expressed as follows

$$\begin{pmatrix} x_{heli} \\ y_{heli} \\ z_{heli} \end{pmatrix} = \begin{pmatrix} x_{gps} \\ y_{gps} \\ z_{gps} \end{pmatrix} + \begin{pmatrix} \Delta x \\ \Delta y \\ \Delta z \end{pmatrix} \quad (4)$$

3.2. *Transformation of image coordinates to global coordinates*

The definition of an image coordinate system (u, v) is shown in *Fig. 5(a)*. This coordinate system has the origin at upper left corner with U axis in the rightward and V axis in the downward. The image coordinate (u, v) are converted to the point (x_H, y_H, z_H) in the helicopter

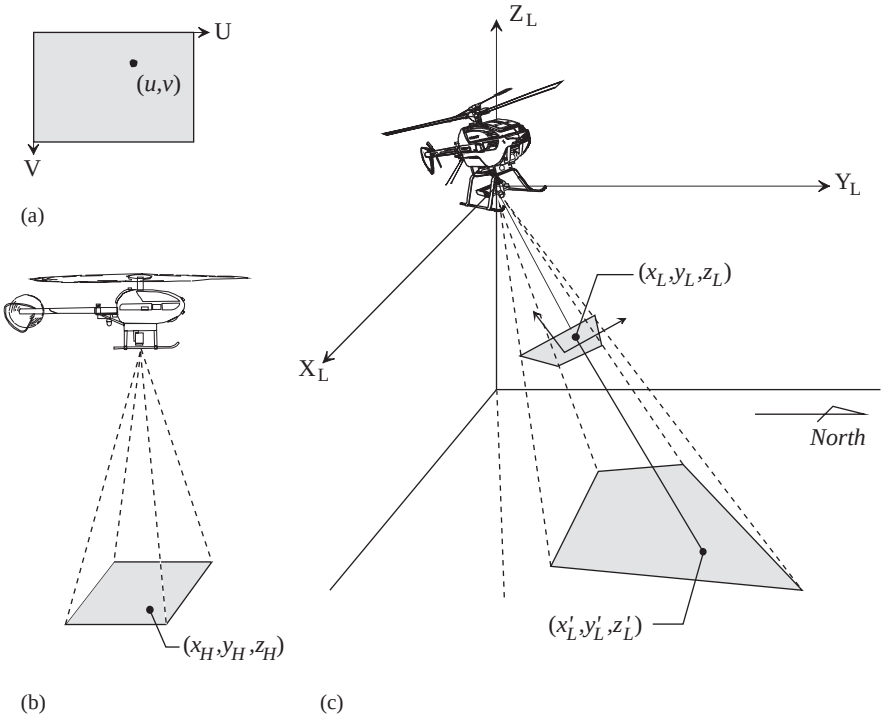

Fig. 5. Transformation from image coordinate to global coordinate: (a) axes for an image coordinate system; (b) conversion from the image coordinates to the helicopter coordinates; (c) image data projection to the ground; (u, v)*, image coordinates of an pixel;* (x_H, y_H, z_H)*, image data position in the helicopter coordinate system;* (x_L, y_L, z_L)*, image data position in the local coordinate system;* (x'_L, y'_L, z'_L)*, projected point in the local coordinate system*

coordinate system as follows [*Fig. 5(b)*]

$$\begin{cases} x_H = u - \bar{u}/2 \\ y_H = \bar{v}/2 - v \\ z_H = -\sqrt{(\bar{u}/2)^2 + (\bar{v}/2)^2}/\tan(\mu/2) \end{cases} \tag{5}$$

In the equations above, $\bar{u}$ and $\bar{v}$ are the resolution of the image with values of 640 and 480, respectively. The value of the diagonal angle of view of the imaging sensor μ is determined as 26·510° through a calibration procedure. Using the developed remote-sensing system, an image taken from an altitude of 30 m covers 11·3 m by 8·5 m of land area with the spatial resolution of 1·8 cm, and an image taken from a height of 70 m height covers 26·4 m by 19·8 m of land area with the spatial resolution of 4·1 cm. It was concluded that spatial resolution is high enough even the helicopter flies at 70 m altitude from the ground.

Also, a local coordinate system (x_L, y_L, z_L) is defined so that its origin equals the optical origin of the imaging sensor, as shown in *Fig. 5(c)*. The point (x_H, y_H, z_H) in the helicopter coordinate system can be transformed to the local coordinates (x_L, y_L, z_L) by using the rotation matrices as shown by

$$\begin{pmatrix} x_L \\ y_L \\ z_L \end{pmatrix} = \boldsymbol{R}_3(\psi)\boldsymbol{R}_2(\theta)\boldsymbol{R}_1(\phi)\boldsymbol{Q}_1(\rho_1)\boldsymbol{Q}_2(\rho_2)\begin{pmatrix} x_H \\ y_H \\ z_H \end{pmatrix} \tag{6}$$

If h is altitude of the helicopter from the ground, (x'_L, y'_L, z'_L) represents the projected point of (x_L, y_L, z_L) to the horizontal plane of $z_L = -h$ in the local coordinate system as follows

$$\begin{pmatrix} x'_L \\ y'_L \\ z'_L \end{pmatrix} = -\frac{h}{z_L}\begin{pmatrix} x_L \\ y_L \\ z_L \end{pmatrix} \tag{7}$$

Therefore, the transformed point of the image data in the global coordinate system, denoted by (x_G, y_G, z_G), can be obtained by adding (x'_L, y'_L, z'_L) to the position of the optical origin of the imaging sensor $(x_{heli}, y_{heli}, z_{heli})$, as shown by

$$\begin{pmatrix} x_G \\ y_G \\ z_G \end{pmatrix} = \begin{pmatrix} x'_L \\ y'_L \\ z'_L \end{pmatrix} + \begin{pmatrix} x_{heli} \\ y_{heli} \\ z_{heli} \end{pmatrix} \tag{8}$$

To test spatial accuracy, 25 markers were put on the ground with a spacing of 5 m. Images were then taken from the helicopter and transformed to the global coordinates using the method above. At this time, the angles of the pan-head were fixed so that the imaging sensor was directed perpendicular to the ground, namely, ρ_1 and ρ_2 were equal to zero. *Figure 6(a)* shows an example of the images, and *Fig. 6(b)* shows the results of the transformation. The centre of the marker was defined as the location of each marker. As this research aims to develop a system that can sense at various altitudes, images were taken from several altitudes and were subsequently used to evaluate spatial accuracy. The mean error between the actual position of the markers and that of the transformed point from the image is shown in Table 1. The range of error was from 1·26 to 2·38 m, resulting from geomagnetic warping of GDS outputs. In addition, errors in the roll and pitch angles also affected the accuracy of the transformation. Results indicated that posture data correction was required before transformation of image data.

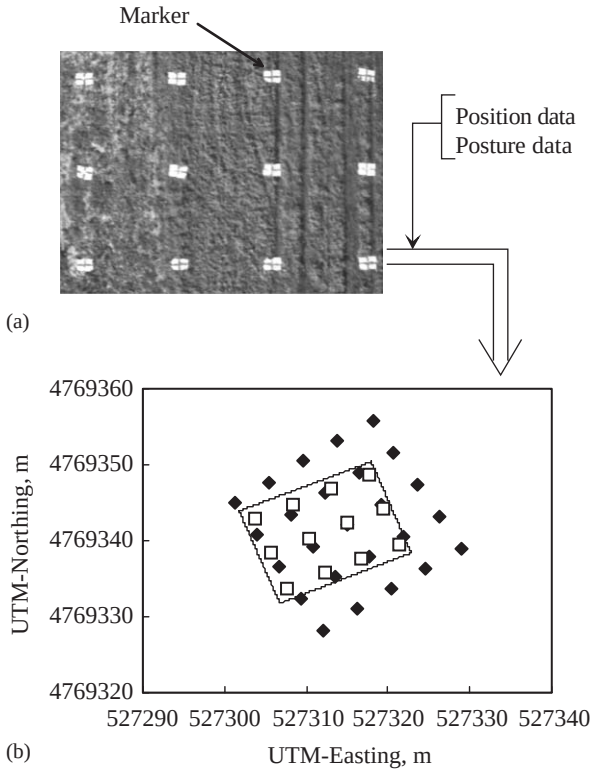

Fig. 6. Result of the image data transformation: (a) the raw image taken from the helicopter; (b) the estimated and actual marker positions: ◆, marker position; □, marker position estimated from image; —, range of the taken image, UTM, universal transverse Mercator

4. Posture data correction

The GDS data contain a large error because of a geomagnetic warp surrounding the helicopter. It was necessary to correct this error to generate a precise field map. To correct the GDS output error, the helicopter was flown in a circle that had a radius of approximately 10 m. GDS data was obtained from the INS during this flight, and a relative direction was obtained from the IMU. The variable ω_{IMU} in Eqn (9) is the relative direction from the IMU, except that the initial value of the IMU was set equal to the GDS output on the initial measurement:

$$\varepsilon = \omega_{IMU} - \psi_{GDS} \tag{9}$$

Since ψ_{GDS} is the GDS output, ε becomes the difference between GDS and IMU outputs. Therefore, ε can be regarded as the error of the GDS. A plot of ε is shown in *Fig. 7*. It can be seen that fluctuation of the GDS error is approximately $\pm 15^\circ$. The curve $f(\psi_{GDS})$ in *Fig. 7* is an approximation described by a Fourier series expansion, Eqn (10).

$$f(\psi_{GDS}) = \sum_{k=0}^{5} a_k \cos(k\psi_{GDS}) + \sum_{k=0}^{5} b_k \sin(k\psi_{GDS}) \tag{10}$$

where a_k and b_k are the Fourier coefficients. Therefore, the true absolute direction ψ_{True} can be expressed as Eqn (11) by introducing a bias error α which equals the initial bias of the IMU:

$$\psi_{True} = \psi_{GDS} + f(\psi_{GDS}) + \alpha \tag{11}$$

The order of Fourier series expansion in Eqn (10) is determined by minimising the final prediction error E_{FP}, which is widely used to determine the order of an

Table 1
Mean error of estimated marker positions based on position and posture data

Image no.	*Mean error, m*	*Altitude, m*	*Roll, deg*	*Pitch, deg*	*Yaw, deg*	*Marker number*
1	1·26	46·78	2·269	0·417	−22·17	12
2	2·38	65·93	−4·801	0·516	−33·025	10
3	1·26	39·52	−3·812	1·395	−21·578	6
4	1·65	63·36	0·983	0·247	−29·832	18
5	1·65	70·75	3·812	2·043	17·512	16

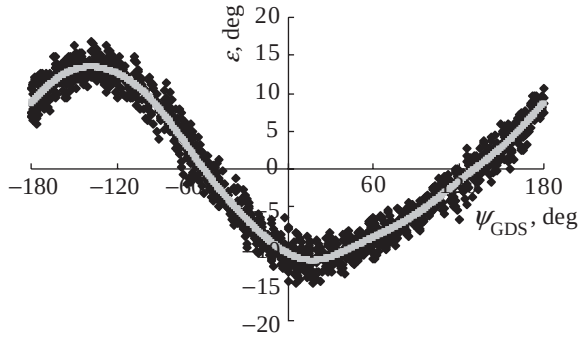

Fig. 7. Fluctuations in the direction error measured by geomagnetic direction sensor (GDS): ■, difference of direction data ε; —, approximate curve; ψ_{GDS}, yaw angle measured by the GDS

auto-regressive model:

$$E_{FP} = \frac{N + 2n}{N - 2n}\,\sigma^2 \tag{12}$$

where: N is the number of the data; n is the order of the Fourier expansion; and σ^2 is the variance of the prediction error.

Figure 8 shows the value of the final prediction error for increasing numbers of Fourier coefficients. The fifth order of the Fourier expansion attains a minimum and was selected.

The better biases for altitude, pitch and roll angles, as well as heading bias α were estimated in order to increase spatial accuracy in the study. This was accomplished by minimising the displacement between actual and estimated marker positions. *Figure 9(a)* shows the mean error and the standard deviation over 62 points in the five images.

To correct the data obtained as an altitude H, a pitch angle θ, and a roll angle ϕ, calculated biases β, γ and δ (for altitude, pitch and roll angles) determine a true posture, Eqn (13):

$$\begin{cases} H_{True} = H + \beta \\ \theta_{True} = \theta + \gamma \\ \phi_{True} = \phi + \delta \end{cases} \tag{13}$$

The effect of β, γ and δ on position error is shown in *Figs 9(b), (c), and (d)*, respectively. The curves in *Fig. 9* show the effect of changing bias error. The 20 bars in each graph show the standard deviation. The bias values with the lowest error were selected: $\alpha = -2{\cdot}110$, $\beta = 0{\cdot}285$, $\gamma = -0{\cdot}520$, $\delta = -0{\cdot}175$.

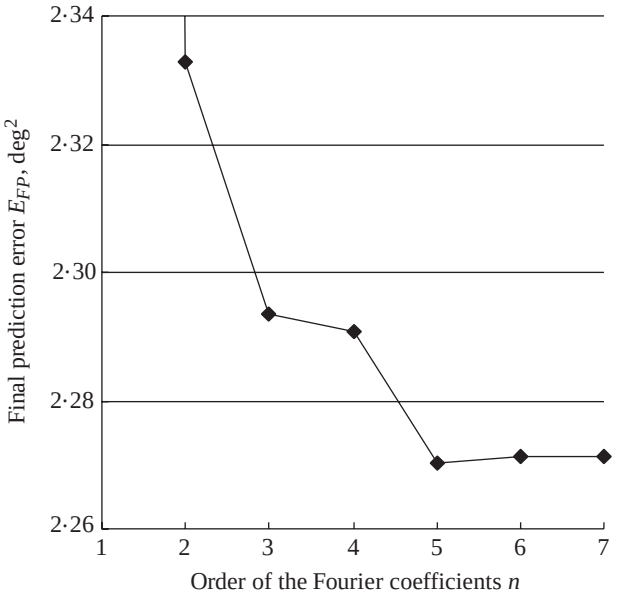

Fig. 8. Final prediction error E_{FP} as a function of the order of Fourier coefficients n

5. Results and discussion

5.1. *Transformation accuracy of image coordinates to ground coordinates*

Figure 10 shows an image transformed by the correction method, where positioning accuracy improved significantly. In all images, the mean error between the actual and estimated marker positions were reduced (Table 2). Estimated markers nearly coincide with actual markers with a mean error from 0·18 to 0·29 m, a significant reduction in spatial error.

5.2. *Reliability of the correction method*

Images 1–5 were used to determine posture bias errors. Other, test images (Images 6–8) were transformed to the global coordinates using the same correction method and biases. The error was from 0·18 m to 0·20 m (Table 3), which is acceptable for sensing crop status.

Five more images (Images 9–13) were taken as test data [*Fig. 11(a)*]. Images 9–13, taken with an adjustable pan-head, were transformed as shown in *Fig. 11(b)*. Transformation accuracy was shown in Table 4, where the error was from 0·28 to 0·38 m. The accuracy of Images 9–13 was lower than that of Images 1–8, resulting from a change in the pan-head angle, especially a tilt angle of approximately 45°. Still, this accuracy

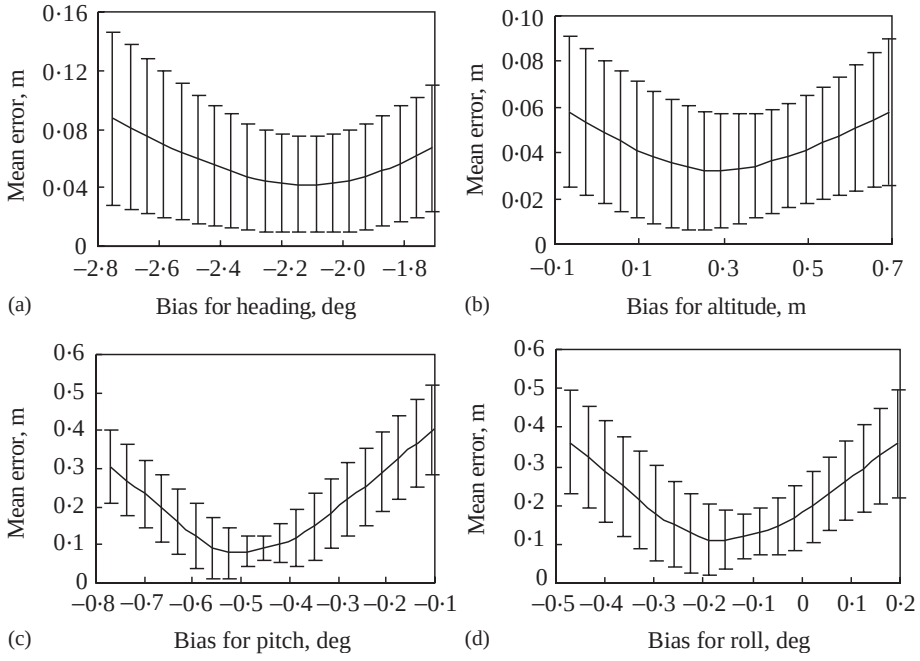

Fig. 9. Mean error for (a) heading angle, (b) altitude, (c) pitch angle, and (d) roll angle biases; —, mean error; I, standard deviation

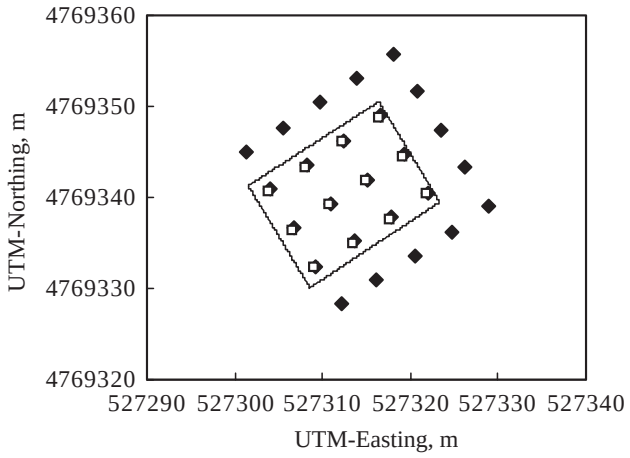

Fig. 10. Improvement of position accuracy using corrected data: ◆, marker position; □, marker position estimated from image; —, range of the taken image, UTM, universal transverse Mercator

Table 2
Mean error of marker positions using corrected posture data

Image no.	*Mean, error, m*
1	0·25
2	0·29
3	0·19
4	0·18
5	0·23

should be acceptable for remote sensing in precision agriculture.

5.3. *Demonstration of mapping system*

A test was carried out in an actual corn field using the developed system. All images obtained were transformed to global coordinate using the previously described correction method. Geographic information system software was used to generate a composite image (*Fig. 12*). As crop rows can be clearly recognised as parallel to each other, GDS image correction was effective. Furthermore, the region of the field in *Fig. 12* was measured using the RTK-GPS. It can be seen that all crop rows in the composite image fit inside the actual region of the field. Individual images in *Fig. 12* were taken every 5 s. All images were captured as multispectral data of R, G and NIR. Average helicopter speed was 0·6 m/s. Considering that crop sensing by the helicopter took only 10 min, a helicopter-based sensing system is much more efficient than a ground-based system. The images were taken from an altitude of 5·5 m to 30 m from the ground. In general, image quality deteriorates as helicopter altitude increases. *Figure 13(a)* shows a raw image taken from an altitude of 30 m at a

Table 3
Mean error of marker positions in test data using position and posture data

Image no.	*Mean error, before correction, m*	*Mean error after correction, m*	*Altitude, m*	*Roll, deg*	*Pitch, deg*	*Yaw, deg*	*Marker number*
6	2·50	0·19	67·61	1·713	2·960	−19·511	16
7	1·03	0·20	31·88	1·719	2·010	−18·012	6
8	1·49	0·18	69·80	−3·098	1·274	−19·627	12

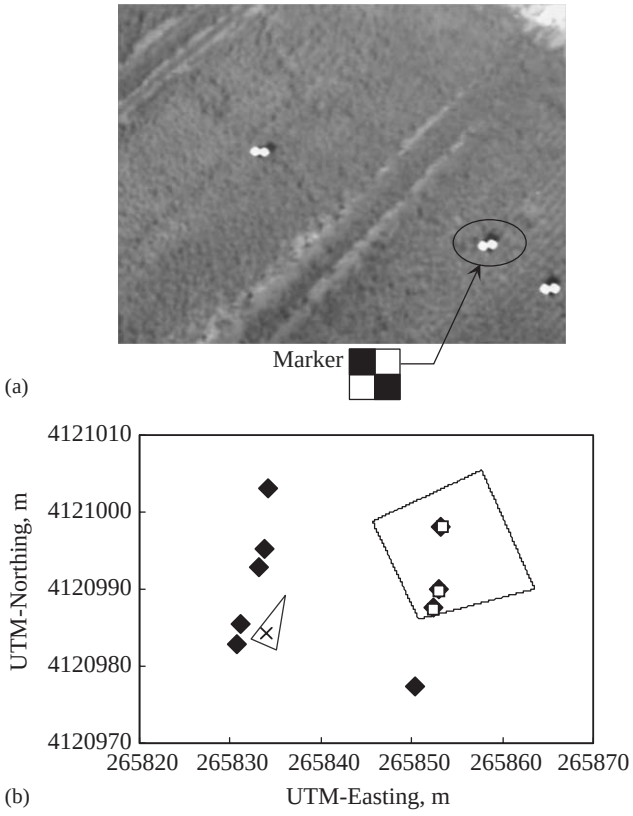

Fig. 11. Result of the image data transformation under changed pan-head angles: (a) the raw image (Image 16) taken from the helicopter; (b) the estimated and actual marker positions: ◆, marker position; □, marker position estimated from image; —, range of the taken image; Δ, helicopter orientation; ×, helicopter position; UTM, universal transverse Mercator

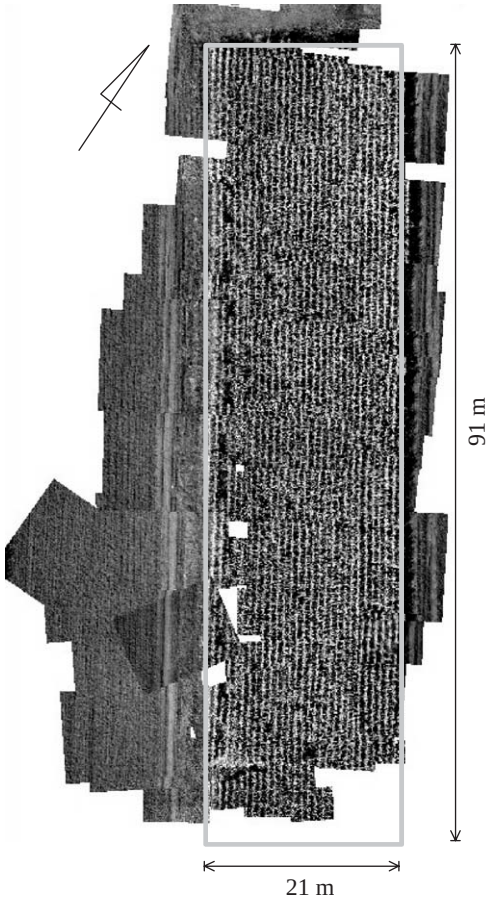

Fig. 12. Composite image of a test maize field: —, actual region of the field

Table 4
Mean error of marker positions using an adjustable pan-head

Image no.	*Mean error, m*	*Altitude, m*	*Roll, deg*	*Pitch, deg*	*Yaw, deg*	*Pan, deg*	*Tilt, deg*	*Marker number*
9	0·36	19·42	3·142	5·478	12·764	1·468	39·720	2
10	0·38	22·00	1·507	2·575	13·394	0·088	44·460	2
11	0·30	33·25	1·109	2·769	30·286	36·808	31·480	3
12	0·28	48·50	4·327	−1·460	18·520	46·108	−2·460	3
13	0·37	51·01	2·785	−0·791	13·151	50·108	−4·800	3

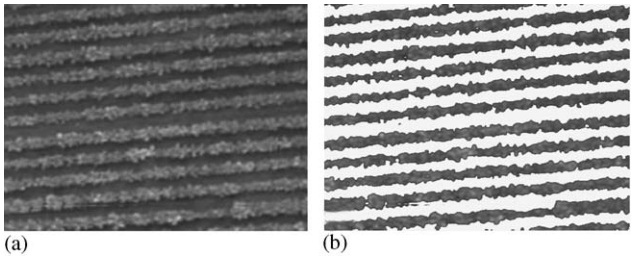

(a) (b)

Fig. 13. Segmentation of the image taken from the unmanned helicopter at a sugar beet field: (a) raw image; (b) segmentation of the soil part in the image

sugar beet field. To evaluate the crop status using LAI, the accurate segmentation of crop and soil area is badly needed. The spatial resolution of an image taken from an altitude of 30 m is about 1·7 cm/pixel. This spatial resolution is still much better than that of satellite or aircraft. The soil part of the image can be successfully segmented as shown in *Fig. 13*(*b*). Therefore, the accurate LAI can be acquired due to the fine resolution image. *Figures 14*(*a*) and (*b*) are crop status maps of the sugar beet field, processed the segmented image

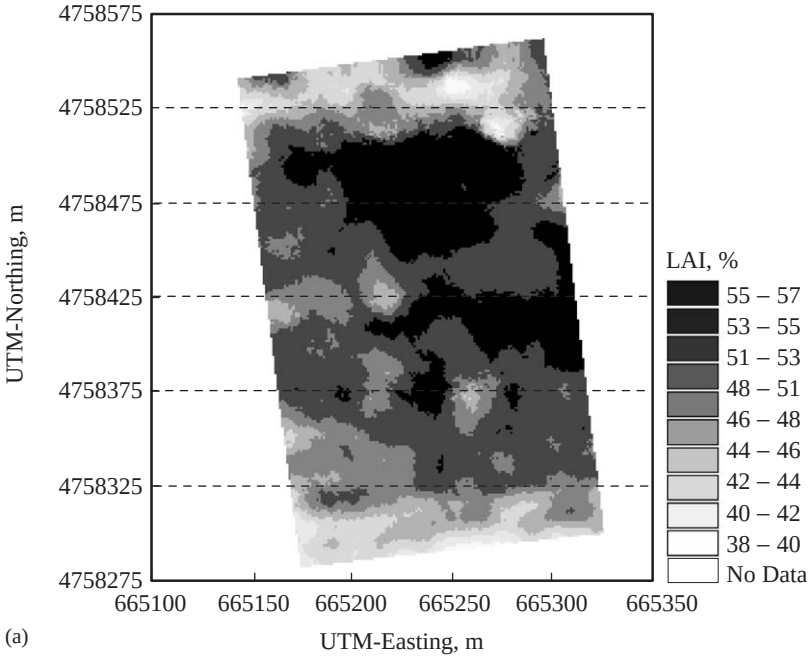

(a)

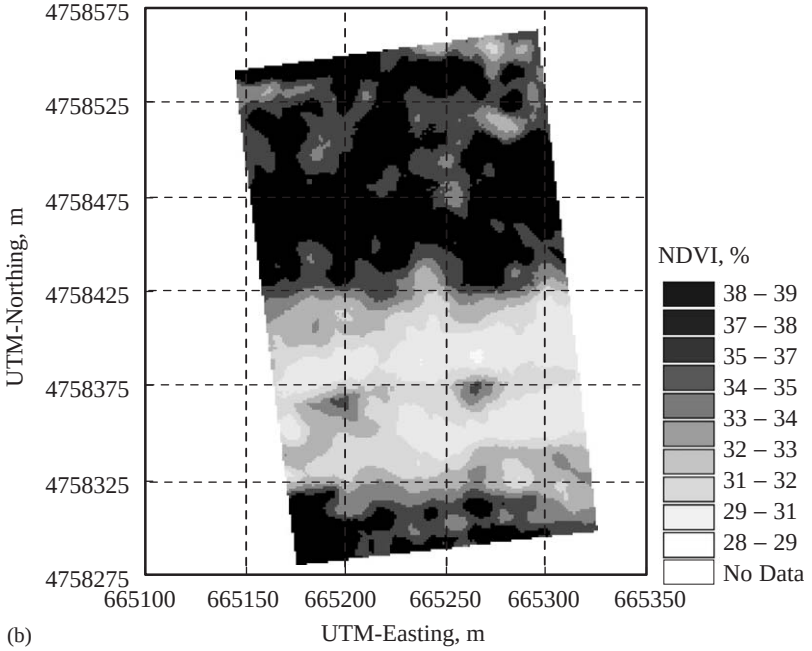

(b)

Fig. 14. Crop status maps of (a) leaf area index (LAI) and (b) normalized vegetation index (NDVI); UTM, universal transverse Mercator

[*Fig. 13*(*b*)]. The LAI and NDVI in vegetation area were calculated and expressed using maps. Since these two values are widely known as crop status indexes, the maps of *Figs 14*(*a*) and (*b*) are useful information for understanding variability of crop growth in a field.

6. Conclusions

A remote-sensing system using an unmanned helicopter was developed in this research. An inertial sensor (INS) and a geomagnetic direction sensor (GDS) were used for measurement of roll, pitch, and yaw angles. A real-time kinematic-global positioning system (RTK-GPS) was adopted as a positioning sensor. The data from these external sources were employed to transform the image coordinates to the global coordinates. The imaging sensor used in the tests was mounted under the fuselage of the helicopter. The geometric distortion of an image due to a variation of the helicopter posture was removed. The GDS correction method by analysis with the relative direction data of an inertial measurement unit (IMU) was developed. Using the developed image correction method, the spatial accuracy of the transformation was evaluated. As a result, the range of the spatial error of the transformation was from 0·18 m to 0·29 m. And the spatial error with pan and tilt angles of about 45° was from 0·28 m to 0·38 m. This accuracy is adequate for geographical information system (GIS) map generation. Also, the map of the corn field was generated by the developed method. However, the GIS map generation system developed in this study is not suitable for a field that has large elevation differences. As sensing a field including slope, the spatial accuracy of the system decreases. Future work includes the development of a three-dimensional mapping system by integrating image data and topographical information of a field.

Acknowledgement

The authors are grateful to the Japan Society of the Promote of Science for the financial support of this study (project #14206029).

References

Agriculture, Forestry, Fishery and Aviation Association (2002). Agriculture, Forestry, Fishery and Aviation Technical Rationalization Examination Results Document. Agriculture, Forestry, Fishery and Aviation Association, Tokyo

Chen S; Huang C; Huang C; Yang C; Wu T; Tsai Y; Miao P (2003). Determination of nitrogen content in rice crop determination of nitrogen content in rice. Proceedings of the 2004 ASAE Annual International Meeting, Paper No. 031132

Gonzalez R; Woods R (1993). Digital Image Processing, (3rd edn.). Addison-Wesley Publishing Company, New York

Hongoh D; Kajiwara K; Honda Y (2001). Developing ground truth measurement system using RC helicopter and BRDF model in forest area. Proceedings of 22nd Asian Conference on Remote Sensing, pp 114–119

Hu B; Qian S; Haboudane D; Miller J R; Hollinger A B; Tremblay N; Pattey E (2004). Retrieval of crop chlorophyll content and leaf area index from decompressed hyperspectral data: the effects of data compression. Remote Sensing of Environment, **92**(2), 139–152

Inoue Y (1997). Remote sensing of crop and vegetative environment (Part 2). Journal of Japan Remote Sensing Society, **17**(4), 57–67

Kato K; Oya A; Karasawa K (1982). Introduction of Aerodynamics. University of Tokyo Press, Tokyo

Lee W; Searcy S (1999). Multispectral sensor for detecting nitrogen in corn plants. Proceedings of the 2000 ASAE Annual International Meeting, Paper No. 001010

Noh H; Zhang Q; Han S (2004). Sensor based variable rate application of nitrogen by using a multi-spectral image sensor. Proceedings of the 2004 ASAE Annual International Meeting, Paper No. 041133

Poli D (2001). Direct georeferencing of multi-line images with a general sensor model. Proceedings of the High Resolution Mapping from Space 2001, published on CD.

Senay G B; Ward A D; Lyon J G; Fausey N R; Nokes S E (1998). Manipulation of high spatial resolution aircraft remote sensing data for use in site-specific farming. Transaction of the ASAE, **41**(2), 489–495

Wong K C (2001). Survey of regional development: civil application. Proceedings of the UAV Australia Conference, pp 8–16

Xu F; Li S (2000). 3D Positioning techniques in airborne laser-ranging and multi-spectral imaging mapping system. Journal of Surveying and Mapping, **29**(2), 137–141

Yang C; Everitt J; Bradford J (2002). Airborne hyperspectral imaging and yield monitoring of grain sorghum yield variability. Proceedings of the 2002 ASAE Annual International Meeting, Paper No. 021079

Yukumoto O; Matuo Y (1996). Measurement of magnetic field. Journal of the Japanese Society of Agricultural Machinery, **58**(5), 93–98